Electrochemical impedance spectroscopy, another arrow in the arsenal to study the biodegradability of two-dimensional materials

Livia Didonè, Yunseok Shin, Alessandro Silvestri, Maurizio Prato, Sungjin Park, Alberto Bianco

Electrochemical impedance spectroscopy, another arrow in the arsenal to study the biodegradability of two-dimensional materials

Livia Didonè,[a] *Yunseok Shin,*[b] *Alessandro Silvestri,*[c,#,*] *Maurizio Prato,*[c,d,e] *Sungjin Park,*[b,*] *Alberto Bianco*[a,*]

[a]CNRS, UPR3572, Immunology, Immunopathology and Therapeutic Chemistry, ISIS, University of Strasbourg, 67000 Strasbourg, France

E-mail: a.bianco@ibmc-cnrs.unistra.fr

[b]Department of Chemistry and Chemical Engineering, Inha University, 100 Inha-ro, Nam-gu, Incheon 22212, Korea

E-mail: sungjinpark@inha.ac.kr

[c]Center for Cooperative Research in Biomaterials (CIC biomaGUNE), Basque Research and Technology Alliance (BRTA), Paseo de Miramón 194, 20014 Donostia San Sebastián, Spain

[d]Ikerbasque, Basque Foundation for Science, 48013 Bilbao, Spain

E-mail: alessandro.silvestri@unive.it

[e]Dipartimento di Scienze Chimiche e Farmaceutiche, INSTM UdR Trieste, University of Trieste Via Licio Giorgieri 1, 34127 Trieste, Italy

[#]Current address: Department of Molecular Sciences and Nanosystems, Ca' Foscari University of Venice, 30170, Venice, Italy

Abstract

Carbon nitride (C_3N_4) is an innovative material with a high potential in many applications including energy storage, catalysis, composites, and biomedicine. C_3N_4 appears remarkably interesting not only for its properties but also because its simple preparation routes involve low-cost starting materials and reagents. However, there is still a lack of information on its degradability. For this reason, in this study, we evaluate the environmental persistence of C_3N_4 and its oxidized form by applying the photo-Fenton reaction. The morphological and structural changes of both materials were monitored by transmission electron microscopy and Raman spectroscopy respectively. In addition, electrochemical impedance spectroscopy has been used as an original technique to validate the degradation process of C_3N_4.

Introduction

Graphitic carbon nitride (C_3N_4), characterized by a triazine or a tris-triazine pattern, is a two-dimensional (2D) material that can be produced from three-dimensional (3D) C_3N_4 via exfoliation. C_3N_4 contains C and N atoms arranged in hexagonal rings made of C=N bond with sp^2 hybridization, resulting in a π-conjugated framework.[1] This class of materials is receiving a lot of interest, not only for its remarkable properties but also because its preparation route involves low-cost starting materials and reagents.[2] In fact, abundant and inexpensive precursors, such as cyanamide, dicyanamide, or urea, can be used. The synthesis of C_3N_4 is performed using a pyrolytic process, consisting of the decomposition of the carbon and nitrogen sources, to produce volatile substances and solid residues. Graphitic carbon nitrides have drawn a lot of attention due to their features, which can be attributed to their layered structure. Besides the simplicity of its synthesis, this material is characterized by high stability, low toxicity, wide visible light absorption range, and an ideal semiconducting behavior. Different C_3N_4 are currently applied for photocatalysis and energy storage.[3,4] For example, they are used as anodic components in rechargeable lithium-ion batteries.[5] Moreover, C_3N_4 can be used as saturable absorber,[6] or in membranes, in solar and fuel cells, and they are effective in removing contaminants from water, air, and soil.[7,8] Since C_3N_4 resulted to be biocompatible, its use in biomedicine, biosensors, for photocatalytic sterilization, photodynamic therapy, and as drug carriers has been exploited.[9] Recently, C_3N_4 was evaluated as an efficient carrier for the anticancer drug cisplatin.[10] Nevertheless, it must always be considered that the interaction of nanoparticles with the biological systems or the environment might generate toxic effects due to their small size, large surface area, and high reactivity. Overall, the physicochemical properties of a nanomaterial have a huge influence on its safety. For example, the degree of dispersion of carbon nanomaterials has an impact on their *in vitro* and *in vivo* toxicity.[11] In order to broaden C_3N_4 applications in the biomedical and other fields, it is fundamental to examine the degradability profiles of this 2D material. The reported cytotoxicity effects of C_3N_4 and other carbon-based nanomaterials include reactive oxygen species generation, DNA damage, lysosomal damage, mitochondrial dysfunction, and eventual cell death via necrosis or apoptosis.[12,13] Cellular assays on lung epithelial cell lines (e.g., A549) showed that for C_3N_4 the toxicity resulted to be dose-dependent, and it was generally rated lower than other 2D materials, such as graphene oxide (GO).[14]

However, no data is available on the (bio)degradability of C_3N_4. Thus, it is crucial to assess the degradability of this type of carbon-based nanomaterials, to foresee and limit their impact on health and the environment. A substance can undergo a mechanical, chemical, or biological degradation process. Biodegradation aims to bio-transform, recycle, and detoxify the concerned material. For example, in the biomedical field, it is crucial to consider the degradation of a therapeutic

nanomaterial, since it should occur at the most proper time and place, namely the targeted pathological site, to allow the pharmacological benefit to take place.[15] Through the years, many studies on carbon-based nanomaterial degradation have been reported, but there is a lack of information regarding the degradability of C_3N_4. Overall, it was demonstrated that carbon-based nanomaterials are sensitive to the treatment with different types of peroxidases, where hydrogen peroxide is involved in the catalytic process. For example, it was shown that the biodegradation of GO by human myeloperoxidase is dispersibility-dependent.[16] Moreover, it was proven that the degradation of GO performed by horseradish peroxidase (HRP) is accelerated and more efficient when GO is functionalized with coumarin or catechol, which are specific ligands of HRP.[17] In this regard, the concept of degradation-by-design has been proposed, where the chemical functionalization of 2D materials enhances their degradability, and, accordingly, their safety.[18] In another study, graphene quantum dots (GQDs) were degraded by myeloperoxidase (MPO) via an oxidative enzymatic process.[19]

Many of the studies focused on the biodegradation of carbon-based nanomaterials are based on the simulation of oxidative conditions, in order to evaluate the behavior of a particular material when it comes in contact with the environment or a living organism. According to the literature, oxidative enzymes such as HRP and MPO are efficient agents for the biodegradation of carbon-based nanomaterials.[20] In addition to enzyme-catalyzed biodegradation, in an environmental context, the photo-Fenton reaction showed also significant results[21] and has been widely used to decompose aromatic organic pollutants in water.[22]

Since there is no sufficient knowledge regarding the degradation of graphitic carbon nitrides, we relied on our previous study conducted on the biodegradation of hexagonal boron nitride (hBN), since this material is known for its chemical inertness and high oxidation resistance.[23] The photo-Fenton reaction was applied as a first approach to study C_3N_4 degradation in environmental conditions. This model reaction was chosen to develop effective tools to monitor the C_3N_4 degradation process, that in future works will be applied to the enzymatic degradation. The photo-Fenton reaction is a UV-assisted version of the Fenton reaction, where the UV light enhances the degradation rate, by accelerating the production of chemically reactive hydroxyl radicals.

The effects of this reaction were monitored by transmission electron microscopy (TEM) imaging and by electrical impedance spectroscopy (EIS). EIS is a novel technique in the study of 2D material degradation, based on the perturbation of an electrochemical system in the equilibrium state, through the application of an oscillating voltage over a wide range of frequencies. The sinusoidal current response is monitored and the resistance of the material is recorded as a function of the perturbation frequency (impedance). EIS is a powerful technique able to discriminate, in the frequency domain,

the electrochemical events occurring contemporarily at the interface between the material and the electrolyte. Therefore, EIS is a unique tool to investigate the changes in the material properties in relation to the surface structure and chemical composition. Based on these principles, EIS is largely used in the study of metal corrosion. Although 2D material degradation is conceptually a similar event, EIS has never been applied in this field.

Results and discussion

In this work, the photo-Fenton reaction was used to assess the biodegradability of two different samples of C_3N_4, corresponding to a material obtained from pyrolysis of urea (termed CN_{Urea}, CN standing for carbon nitride) and to a material prepared from pyrolysis of melamine followed by the Hummers' treatment to obtain a material rich on oxygenated functions (termed $oxCN_{Mel}$). CN_{Urea} was obtained as a pale-yellow powder by thermal polycondensation of urea at 550 °C under a flow of air/H_2O gas (Scheme 1).[24]

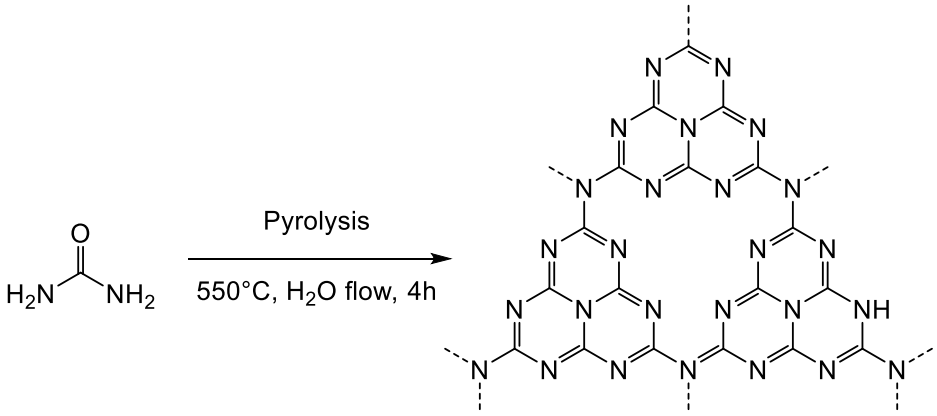

Scheme 1.Synthesis of CN_{Urea}.

The second sample ($oxCN_{Mel}$) was synthesized by a two-step process starting from melamine. Heat treatment of melamine generated carbon nitride materials, followed by a chemical modification using H_2SO_4 and $KMnO_4$ as strong oxidizing reagents, afforded $oxCN_{Mel}$ (Scheme 2). The purpose was to obtain a material that would be easier to degrade, owing to the presence of the oxygenated functions. We point out that it was not possible to obtain this oxidized form of carbon nitride from CN_{Urea} because this latter is too sensitive to strong acidic conditions, which lead to complete degradation during the oxidation process. This can be considered a novel route to produce small sheets of water-dispersible and atomically thin oxidized carbon nitride-based materials.[25]

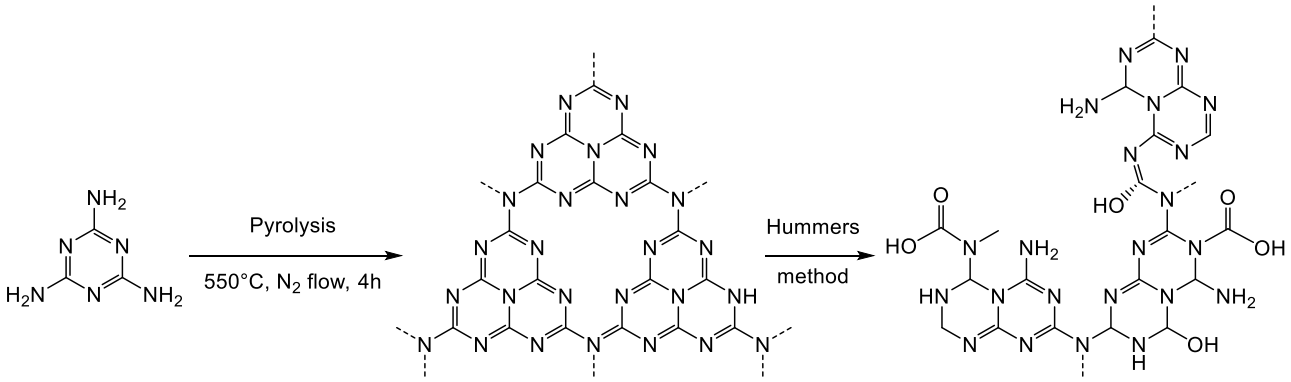

Scheme 2. Synthesis and proposed structure of $oxCN_{Mel}$.

Both CN_{Urea} and $oxCN_{Mel}$ were characterized using complementary spectroscopic and microscopic techniques (see data and discussion in ESI, Figure S1-S7). The characterizations revealed that CN_{Urea} contains tri-s-triazine-based crystalline C_3N_4 structures, while $oxCN_{Mel}$ contains heavily oxidized C_3N_4-based structures with significantly damaged sp^2 networks.

For the degradability studies, stock water dispersions (0.78 mg/mL) were prepared using a cup-horn sonicator, operating for 60 min. The photo-Fenton reaction was then applied by incubating the dispersions of the two materials in an acidic aqueous solution, where $FeCl_3$ and H_2O_2 were regularly added as catalysts. In acidic conditions, Fe^{3+} mainly exists as $Fe(OH)^{2+}$, and effectively absorbs UV light. In this way, a disproportionation occurs being $Fe(OH)^{2+}$ transformed into Fe^{2+} and hydroxyl radicals, that generate the oxidation conditions of the materials (Figure S8). The process is accelerated by UV irradiation at a wavelength of 365 nm. The reaction to degrade both carbon nitride materials was carried out for 100 h at room temperature, by renewing $FeCl_3$ every 35 h and H_2O_2 every 10 h. TEM is commonly employed to follow the progress of the nanomaterial degradation,[20] even though this technique provides qualitative rather than quantitative results. Before starting the degradation process, CN_{Urea} appears round shaped and organized as layered structures. Despite the long sonication process, the particles are not homogeneously distributed on the grid, but they are present as aggregates (Figure 1).

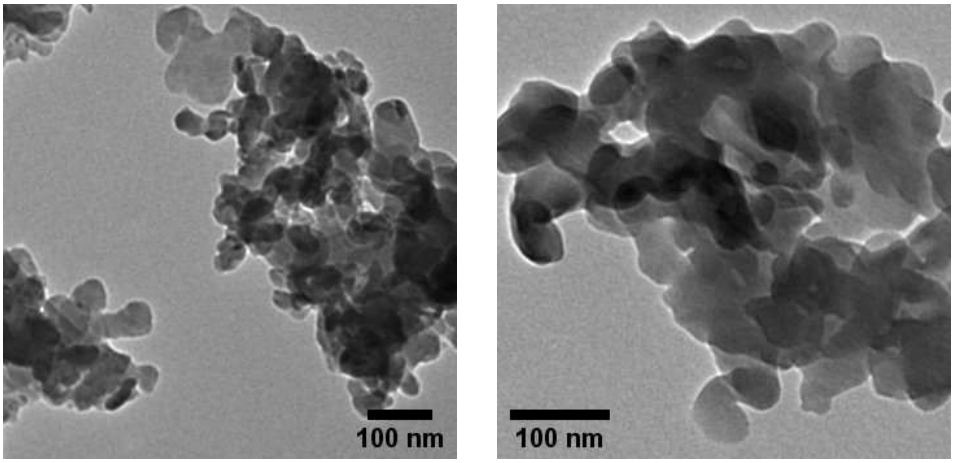

Figure 1. TEM images of CN_{Urea} dispersed in water.

TEM images of the samples were captured at different time points. To monitor the process of degradation on the material, and to obtain significant information about the morphological changes, the samples were observed first after 50 h (Figure 2). At this time point, some pores inside the structure started forming, but it is after 100 h that the edges appear jagged and the number of holes in the material becomes more significant (Figure 3).

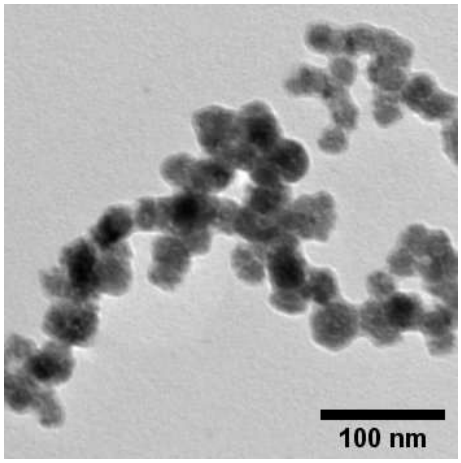

Figure 2. TEM images of CN_{Urea} after 50 h treatment.

We already proved that the treatment of hBN for 100 h in the conditions of the photo-Fenton reaction resulted in the successful degradation of the material, since its 2D layered structure was completely lost at the end of the process. During this experiment with C_3N_4, we expected to achieve a similar result in the same time frame. However, even if the TEM images allow us to state that the oxidation process has modified the material, the degradation was not completed.

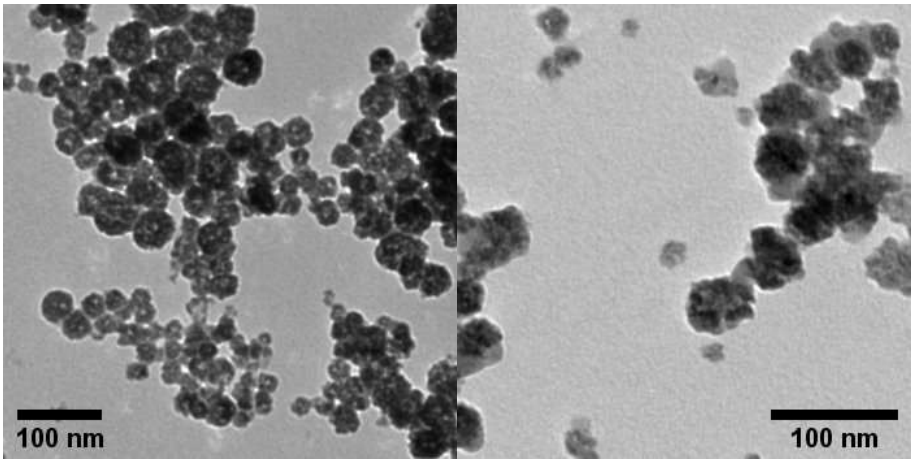

Figure 3. TEM images of CN_{Urea} after 100 h treatment.

The TEM analysis of $oxCN_{Mel}$ before degradation, evidenced a less homogeneous material, with many irregular layers surrounding one another (Figure 4).

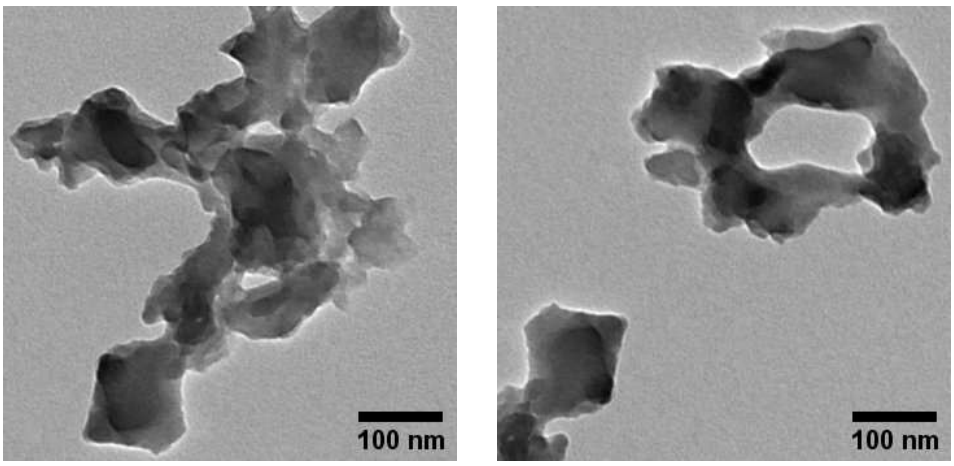

Figure 4. TEM images of $oxCN_{Mel}$ dispersed in water.

To evaluate the degradation of $oxCN_{Mel}$, the samples were observed again after 50 and 100 h of reaction. In the middle of the process, no significant changes were visible (Figure 5, left**Figure *5***). However, at the end of the photo-Fenton reaction, the morphology of the material showed evident modifications (**Erreur ! Source du renvoi introuvable.**, right**Erreur ! Source du renvoi introuvable.**). In facts, there are holes inside the structure, and the edges appear fragmented.

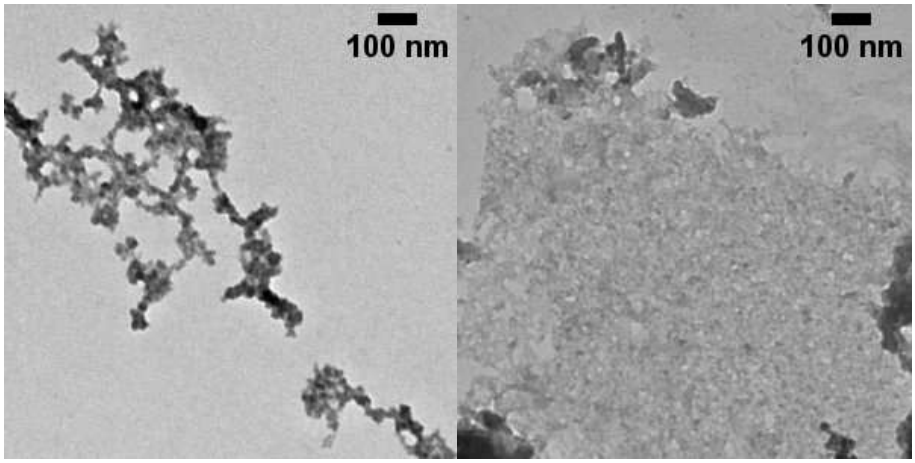

Figure 5. TEM images of $oxCN_{Mel}$ after 50 (left) and 100 h (right) treatment.

Overall, for both materials, the results of the TEM analysis show an incomplete degradation of the starting material by the end of the experiments. This suggests that the degradation took place, but only partially. Moreover, inspired by the study of hBN degradation,[23] Raman spectroscopy was considered as an additional characterization technique to follow the degradation process. This kind of spectroscopy is known to be remarkable not only for being nondestructive, fast and high-resolution, but also for its ability to provide a comprehensive overview of the structural electronic information of a material.[26] Carbon-based nanomaterials present diagnostic bands in the Raman spectrum that correspond directly to a specific vibrational frequency of a molecular bond. During the degradation process, it is likely to observe the decrease in intensity of these distinguishing peaks. For example, a complete disappearance of the band was seen at the end of the photo-Fenton degradation of hBN.[23] In the case of C_3N_4 both in powder and on the residue obtained depositing and drying the solution on a silica wafer, CN_{Urea} and $oxCN_{Mel}$ revealed a very strong autofluorescence, which hampered the observation and evolution of their characterizing peaks during the photo-Fenton process (Figure S9). Although TEM allowed to see the onset of the biodegradation process of these two types of carbon nitrides, the need to broaden the understanding of this phenomenon was relevant. To this aim, EIS proved to be effective. EIS is an electrochemical technique used to study the phenomena happening at the interface of an electrode and a solution of electrolyte. When an electrode is immersed in an electrolyte and polarized, a series of phenomena take place at the liquid-solid interface. Some of the main phenomena involved include the formation of an electrical double layer at the interface, charge transfer through the materials, and the diffusion of chemical species from the bulk of the electrolyte to the surface.[27] Although all these phenomena take place at the same time, EIS can resolve them by applying an oscillating potential to the electrode and measuring the impedance in function of the frequency. The contribution of each of these processes depends on the chemical composition of the material at the interface and on its morphology.[28] The photo-Fenton reaction is expected to degrade

C_3N_4 modifying its morphology, oxidation degree and introducing defects in the crystalline structure affecting the behavior of the material at the interface with an electrolyte solution. To confirm our hypothesis and prove that EIS can be used to study the degradation of 2D materials, we drop-cast aliquots of the two types of C_3N_4 on top of a glassy carbon electrode (GCE), sampled at time 0 and 100 h of the photo-Fenton reaction. Potassium ferricyanide ($K_3[Fe(CN)_6]$) was used as an electrochemical mediator to investigate the phenomena happening at the interface with the material. $E_{1/2}$ of $K_3[Fe(CN)_6]$ (0.21V) was selected as operational potential, as at this potential the mediator generates a faradaic current, which is exploited to study the properties of the material. Small perturbations of 10 mV were applied with a range of frequencies between 100 kHz and 10 mHz. In Figures 6A and 6C it is possible to see the Bode plots for CN_{Urea} and $oxCN_{Mel}$, representing the impedance of the material in function of applied frequency. At high frequencies (up to 1 kHz) the value of impedance is constant and does correspond to the uncompensated resistance of the electrochemical system. In the middle region, we can see an increase in the impedance due to the charge transfer process across the material. Finally, the rapid increase in the impedance at low frequencies can be attributed to the formation of a depletion layer, due to the consumption of the mediator close to the electrode surface. When this happens, the value of impedance is governed by the diffusion rate of the electrochemical mediator from the bulk of the solution to the surface of the electrode.[28]

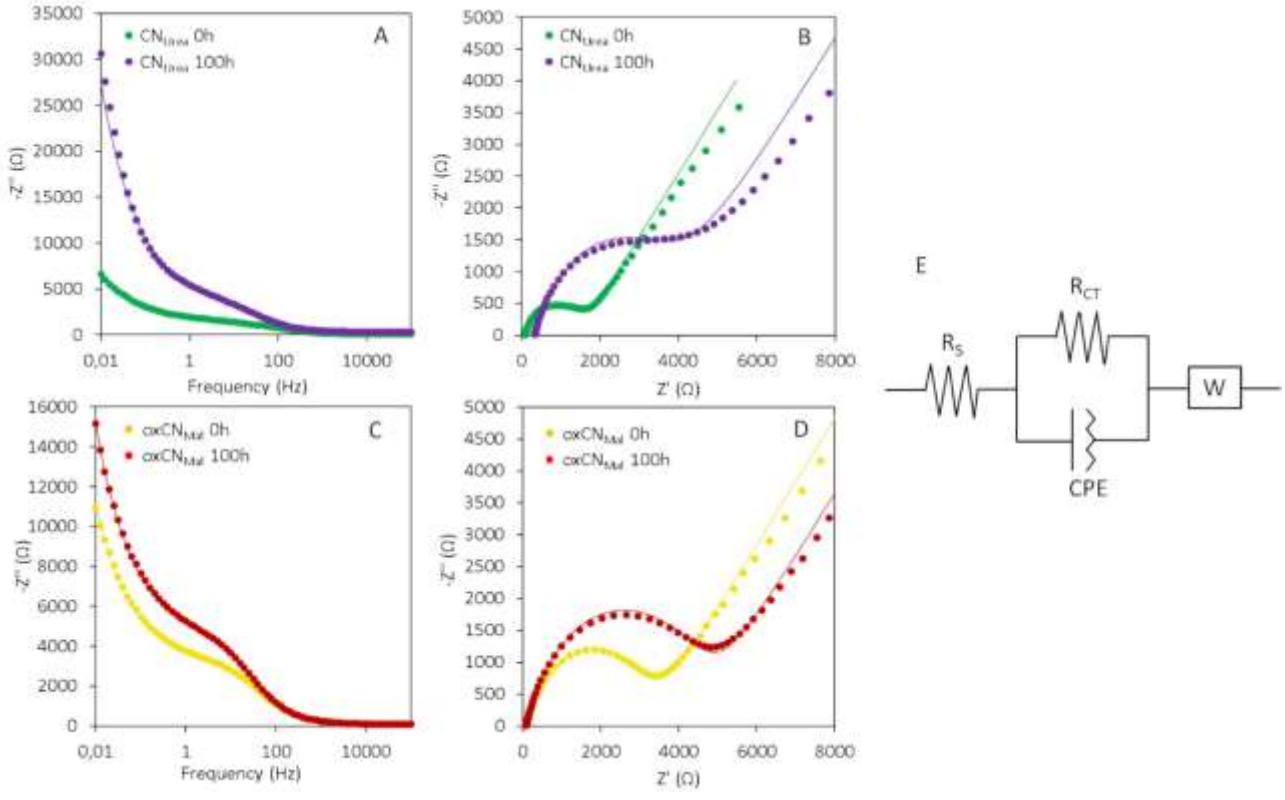

Figure 6. EIS measurements were obtained by drop casting 1 mg/ml of C_3N_4 on a GCE electrode, in a solution of 5 mM of $K_3[Fe(CN)_6]$. A potential of 0.21 V (vs. reference) was applied with a perturbation of 10 mV in a range of frequencies between 100 kHz and 10 mHz. A) Bode plot of CN_{Urea} before (0 h) and after (100 h) the photo-Fenton reaction. The dots represent the experimental data, and the line is the fitting. B) Nyquist plot of CN_{Urea} before (0 h) and after (100 h) the photo-Fenton reaction. C) Bode plot of $oxCN_{Mel}$ before (0 h) and after (100 h) the photo-Fenton reaction. D) Nyquist plot of $oxCN_{Mel}$ before (0 h) and after (100 h) the photo-Fenton reaction. E) Scheme of the equivalent circuit used to fit the EIS data.

In case of both CN_{Urea} and $oxCN_{Mel}$, higher values of impedance were recorded for the samples which underwent the photo-Fenton reaction. However, for $oxCN_{Mel}$ the difference is less pronounced, as the starting material was already oxidized and presented a higher impedance compared to $CN_{Urea.}$ The Nyquist plots (Figure 6B and 6D) represent the imaginary (Z'') part of the impedance plotted as a function of the real one (Z'). These graphs give a good visual interpretation of the phenomena taking place at the interface of the electrode. The semicircle at the beginning of the curve confirms the presence of a charge transfer process. The larger is the diameter of the semicircle, the higher is the resistance of the material at the electron transfer. The tail of the curve with a slope of 45° is representative of the diffusion processes taking place from the bulk of the solution to the interface. From the Nyquist plot, it is possible to extrapolate quantitative data, by fitting it with an equivalent circuit. The circuit chosen in this work is represented in Figure 6E and is composed of a parallel resistance and a constant phase element (CPE) in series with a Warburg (W) element. R_S represents the uncompensated resistance. R_{CT} represents the resistance to electron transfer imposed by C_3N_4. CPE is an imperfect capacitor and represents the formation of a double layer of charges at the interface with the electrolyte. Finally, W is a mathematical equation representing the diffusive process. The most significant value that can be obtained from the fitting is the R_{CT}. For CN_{Urea}, R_{CT} increases drastically after the photo-Fenton process from 1.38 kΩ to 3.06 kΩ indicating that the reaction induces the formation of defects and oxidized sites in the carbon nitride structure, and therefore can partially degrade it. Due to the Hummers oxidative process, the charge transfer resistance of the $oxCN_{Mel}$ is instead high already before the photo-Fenton reaction (3.1 kΩ). Control reactions without Fe, H_2O_2, or UV light treatment were performed. In the three cases no variation of the resistance was detected, confirming that in the absence of one of the three factors the degradation does not take place (Figure S10). The evolution in time of the C_3N_4 degradation process was investigated by taking aliquots from the reaction mixture at the time points 20 h and 50 h (Figure S11). Due to the reduced volume of the aliquots, less material was available to perform these time-resolved measurements.

Consequently, we drop cast 10 µl of 0.1 mg/ml C_3N_4 solution on the GCE. The lower amount of C_3N_4 deposited resulted in higher charge transfer resistance values. Nevertheless, the trend seen in Figure 6 is confirmed: the resistance to the charge transfer of both CN_{Urea} and $oxCN_{Mel}$ increases with time, corroborating that this effect is correlated with progressive material degradation. Furthermore, these data confirm that the changes in R_{CT} for $oxCN_{Mel}$ are less prominent, since the oxidized material presents higher charge resistance values before the photo-Fenton reaction.

In summary, the results of TEM and EIS evidenced a partial degradation of the two carbon nitrides during the course of the photo-Fenton reaction. While the onset of CN_{Urea} biodegradation was clearly demonstrated, the morphological changes in $oxCN_{Mel}$ were more difficult to assess. This is likely because the initial oxidation of this material already disrupted its graphitic structure, resulting in a difficult distinction of the contribution of the Hummers reaction from the oxidative degradation operated by the photo-Fenton reaction. In conclusion, the synergy between the two spectroscopic and microscopic methods used in this study contributed to a better understanding the degradation process of graphitic carbon nitrides and could be applied to other 2D materials.

CRediT authorship contribution statement

AB, AS and SP planned the experiments. LD, YS and AS carried out the experiments. LD, YS, AS and AB analyzed the data. AB, SP and MP searched for funding. LD, YS, AS, SP and AB wrote the manuscript. All authors read and commented the manuscript.

Acknowledgments

We gratefully acknowledge the financial support from PHC STAR Program 2022 (Project 47404TA), Centre National de la Recherche Scientifique (CNRS), Jean-Marie Lehn Foundation, and Interdisciplinary Thematic Institute SysChem via the IdEx Unistra (ANR-10-IDEX-0002) within the program Investissement d'Avenir. The authors are indebted to Cathy Royer from the Plateforme Imagerie In Vitro de l'ITI Neurostra for SEM analyses. S. Park and Y. Shin were supported by National Research Foundation of Korea (NRF) grants funded by the Korean government (MSIT) (NRF-2021R1A2B5B02001587 and 2021K1A3A1A21039034). LD wish to thank the Erasmus+ Program from the University of Trieste (Italy). We also thank L. Jacquemin, R. Soltani, Y. He and I. Janica for their help on XPS and Raman analyses.

References

1) N. Baig, *Compos. Part A* 2023, **165**, 107362.

2) T. K. Mukhopadhyay, L. Leherte and A. Datta, *J. Phys. Chem. Lett.*, 2021, **12**, 1396–1406.

3) C. Rosso, G. Filippini, A. Criado, M. Melchionna, P. Fornasiero and M. Prato, *ACS Nano*, 2021, 15, 3621–3630.

4) G. Filippini, F. Longobardo, L. Forster, A. Criado, G. Di Carmine, L. Nasi, C. D'Agostino, M. Melchionna, P. Fornasiero and M. Prato, *Sci. Adv.* 2020, **6**, eabc9923.

5) T. S. Miller, A. B. Jorge, A. Sella, F. Corà, P. R. Shearing, D. J. L. Brett and P. F. McMillan, *Electroanalysis*, 2015, **27**, 2614–2619.

6) M. Wang, F. Ma, Z. Wang, D. Hu, X. Xu and X. Hao, *Photonics Res.*, 2018, **6**, 307.

7) D. Jang, S. Lee, N. H. Kwon, T. Kim, S. Park, K. Y. Jang, E. Yoon, S. Choi, J. Han, T. W. Lee, J. Kim, S. J. Hwang and S. Park, *Carbon*, 2023, **208**, 290–302.

8) D. Jang, S. Park, S. Choi, J. Kim and S. Park, *J. Photochem. Photobiol. A Chem.*, 2023, **443**, 114840.

9) S. Che, L. Zhang, T. Wang, D. Su and C. Wang, *Adv. Sustainable Syst.*, 2022, **6**, 2100477.

10) M. Perveen, S. Nazir, A. W. Arshad, M. I. Khan, M. Shamim, K. Ayub, M. A. Khan and J. Iqbal, *Biophys. Chem.*, 2020, **267**, 106461.

11) X. Yuan, X. Zhang, L. Sun, Y. Wei and X. Wei, *Part. Fibre Toxicol.* 2019, **16**, 18.

12) H. Taheri, M. A. Unal, M. Sevim, C. Gurcan, O. Ekim, A. Ceylan, Z. Syrgiannis, K. C. Christoforidis, S. Bosi, O. Ozgenç, M. J. Gómez, M. Turktas Erken, Ç. Soydal, Z. Eroğlu, C. V. Bitirim, U. Cagin, F. Arı, A. Ozen, O. Kuçuk, L. G. Delogu, M. Prato, Ö. Metin and A. Yilmazer, *Small*, 2020, **19**, 1904619.

13) B. Fadeel, C. Bussy, S. Merino, E. Vázquez, E. Flahaut, F. Mouchet, L. Evariste, L. Gauthier, A. J. Koivisto, U. Vogel, C. Martín, L. G. Delogu, T. Buerki-Thurnherr, P. Wick, D. Beloin-Saint-Pierre, R. Hischier, M. Pelin, F. Candotto Carniel, M. Tretiach, F. Cesca, F. Benfenati, D. Scaini, L. Ballerini, K. Kostarelos, M. Prato and A. Bianco, *ACS Nano*, 2018, **12**, 10582–10620.

14) Q. Dong, N. Mohamad Latiff, V. Maza, N. Farhanah Rosli, H. Ling Chia and M. Pumera, *ACS Appl. Nano Mater.*, 2018, **1**, 4442–4449.

15) R. R. Remya, A. Julius, T. Y. Suman, V. Mohanavel, A. Karthick, C. Pazhanimuthu, A. V. Samrot and M. Muhibbullah, *J. Nanomater.*, 2022, **2022**, 6090846.

16) R. Kurapati, J. Russier, M. A. Squillaci, E. Treossi, C. Ménard-Moyon, A. E. Del Rio-Castillo, E. Vazquez, P. Samorì, V. Palermo and A. Bianco, *Small*, 2015, **11**, 3985–3994.

17) R. Kurapati, F. Bonachera, J. Russier, A. R. Sureshbabu, C. Ménard-Moyon, K. Kostarelos and A. Bianco, *2D Mater*, 2018, **5**, 015020.

18) A. R. Sureshbabu, R. Kurapati, J. Russier, C. Ménard-Moyon, I. Bartolini, M. Meneghetti, K. Kostarelos and A. Bianco, *Biomaterials*, 2015, **72**, 20–28.

19) C. Martín, G. Jun, R. Schurhammer, G. Reina, P. Chen, A. Bianco and C. Ménard-Moyon, *Small*, 2019, **15**, 1905405.

20) B. Ma, C. Martín, R. Kurapati and A. Bianco, *Chem. Soc. Rev.*, 2020, **49**, 6224–6247.

21) X. Luan, C. Martín, P. Zhang, Q. Li, I. A. Vacchi, L. G. Delogu, Y. Mai and A. Bianco, *Angew. Chem. Int. Ed.*, 2020, **59**, 18515–18521.

22) X. Zhou, Y. Zhang, C. Wang, X. Wu, Y. Yang, B. Zheng, H. Wu, S. Guo and J. Zhang, *ACS Nano*, 2012, **6**, 6592–6599.

23) R. Kurapati, C. Backes, C. Ménard-Moyon, J. N. Coleman and A. Bianco, *Angew. Chem. Int. Ed.*, 2016, **55**, 5506–5511.

24) D. Jang, S. Choi, N. H. Kwon, K. Y. Jang, S. Lee, T. W. Lee, S. J. Hwang, H. Kim, J. Kim and S. Park, *Appl. Catal. B*, 2022, **310**, 121313.

25) J. Oh, R. J. Yoo, S. Y. Kim, Y. J. Lee, D. W. Kim and S. Park, *Chem. Eur. J.*, 2015, **21**, 6241–6246.

26) A. C. Ferrari, *Solid State Commun.*, 2007, **143**, 47–57.

27) E. Barsoukov and J. R. Macdonald, *Impedance Spectroscopy: Theory, Experiment, and Applications*, 2018, John Wiley & Sons, Inc.

28) W. Hu, Y. Peng, Y. Wei and Y. Yang, *J. Phys. Chem. C*, 2023, **127**, 4465–4495.

Electrochemical impedance spectroscopy, another arrow in the arsenal to study the biodegradability of two-dimensional materials

*Livia Didonè,[a] Yunseok Shin,[a] Alessandro Silvestri,[c,#] Maurizio Prato,[c,d] Sungjin Park,[b] Alberto Bianco[a,]**

[a]CNRS, UPR3572, Immunology, Immunopathology and Therapeutic Chemistry, ISIS, University of Strasbourg, 67000 Strasbourg, France

E-mail: a.bianco@ibmc-cnrs.unistra.fr

[b]Department of Chemistry and Chemical Engineering, Inha University, 100 Inha-ro, Nam-gu, Incheon 22212, Korea

[c]Center for Cooperative Research in Biomaterials (CIC biomaGUNE), Basque Research and Technology Alliance (BRTA), Paseo de Miramón 194, 20014 Donostia San Sebastián, Spain

[d]Ikerbasque, Basque Foundation for Science, 48013 Bilbao, Spain

ELECTRONIC SUPPLEMENTARY INFORMATION

Materials and methods

Synthesis of CN_{Urea}

Urea (1 g, 99.0%, Sigma-Aldrich) was added to an alumina crucible then the crucible was put in a quartz tube furnace (TFP-80-3, Dongseo Science Co., Ltd., south Korea). The furnace was filled with air/H_2O gas, and the temperature was elevated to 550 ℃ with a heating rate of 10 ℃/min. The temperature was held at 550 ℃ for 4 h under a flow of air/H_2O gas. The product (CN_{Urea}, 93 mg) was obtained as yellowish powder.

Synthesis of $oxCN_{Mel}$

Melamine (1 g, 99%, Sigma-Aldrich) was added to an alumina crucible then the crucible was put in a quartz tube furnace. The furnace was filled with N_2 gas and the temperature was elevated to 550 ℃ with a heating rate of 10 ℃/min. The temperature was held at 550 ℃ for 4 h under a flow of N_2 gas. The product (CN_{Mel}, 264 mg) was obtained as yellowish powder.

CN_{Mel} (4 g) was added to a flask filled with H_2SO_4 (100 mL, 95%, Daejung). Then $KMnO_4$ (4.28 g, 99.3%, Daejung) was then slowly added to the flask in an ice-bath. The mixture was stirred for 2 h at 35 ℃ then excess water was added to the mixture in an ice-bath. H_2O_2 (35%, Junsei) was then slowly added to the mixture at 25 ℃ until no gas was evolved. The resulting mixture was filtered, washed with 1 L of 5% HCl solution followed by water-washing several times. After drying under vacuum at 25 ℃ for 12 h, $oxCN_{Mel}$ (48 mg) was obtained.

Degradation protocol of the photo-Fenton reaction

In quartz tubes has been put 0.31 mL material (CN_{Urea} and $oxCN_{Mel}$) in aqueous solution (0.78 mg/mL), 10 µL of 1 mM $FeCl_3 \cdot 6H_2O$, 2.46 mL of H_2O. Then the solution was adjusted with 0.1 M HCl, to obtain pH 4. Every 10 hours 50 µL of 100 mM H_2O_2 were injected. Every 35 hours there was the addition of 10 µL of 1 mM $FeCl_3 \cdot 6H_2O$. The reaction has been carried out for 100 hours, taking aliquots of 50 µL at times 0 h, 20 h, 50 h, and 100 h, stored at -20 °C in the dark until characterization by different techniques. Three control reactions containing 0.31 mL of material (0.78 mg/mL) and 2.46 mL of water were performed under the UV lamp, without the use of all the other catalysts.

Transmission electron microscopy

For the TEM characterizations, 6 µL of each solution has been deposited on carbon-coated copper grids, dried and analyzed on a Hitachi H7500 microscope (Tokyo, Japan) with an accelerating voltage of 80kV, equipped with an AMT Hamamatsu camera (Tokyo, Japan). TEM images in SI were obtained using a field-emission transmission electron microscope (JEM2100F, JEOL, Japan) at 200 kV using a carbon/copper holey grid (HC200eCu, EMS, USA).

Raman spectroscopy

Raman analysis of all the samples was performed using Raman spectra Renishaw inVia microRaman, equipped with 532 nm laser and a Leica microscope.

X-Ray photoelectron spectroscopy

XPS was performed on a K-ALPHA Surface Analysis Spectrophotometer (Thermo Scientific) with a basic chamber pressure of 10^{-8}-10^{-9} bar and an Al anode as X-Ray source (1486 eV). For each sample, three spectra were collected. The powder of the raw materials, pressed on copper scotch tape, was analyzed. To check the trends of the different degradation reactions, the samples were prepared by drop-casting on a Silica wafer (4 µL drop, repeated 3 to 4 times to reach a sufficient thickness). A spot size of 400 µm was chosen for the analysis. The survey spectra were the result of the average of 10 scans with a pass energy of 200.00 eV and a step size of 1 eV. The high-resolution spectra were an average of 10 scans with a pass energy of 50 eV and a step size of 0.1 eV. An electron flood gun was working during the analysis as a charge neutralizer. Deconvolution parameters: C1s spectra were deconvoluted in C=O/C=N (287.6-289.9 eV), which are partially overlapping one another; C-O/C-N (286.2-287.2 eV), in this case, was considered a range of error too, since the binding energies of the two types of bonds were overlapped; C-C (284.4-285.3 eV) for sp^2 and sp^3 carbon atoms. For data analysis casaXPS (2.3.18) software was used: A Shirley background subtraction was applied; a lineshape 70% Gaussian/30% Lorentzian [GL(30)] was selected; the FWHM was constrained to be the same for all peaks, apart from the pi*peak because it is a broad signal, and for the C-N/C-S bond because this peak overlapped with C-O and C-C.

X-ray diffraction

XRD patterns were measured using a DMAX-2500 diffractometer (Rigaku, Tokyo, Japan).

Fourier transform infrared spectroscopy

FT-IR spectra were obtained from KBr pellets containing the samples using an FT-IR vacuum spectrometer (Bruker VERTEX 80 V, Bruker, Germany).

Photoluminescence

PL spectra (f = 0.5 m, Acton Research Co., Spectrograph 500i, USA) were performed at room temperature with a 300 nm diode-pumped solid-state laser excitation using an intensified charge-coupled device (PI-MAX3) (Princeton Instrument Co., IRY1024, USA)

Electrical impedance spectroscopy

EIS was registered using an Autolab MSTAT204 potentiostat/galvanostat (Metrohm). A three-electrode configuration, composed by GCE as a working electrode (WE), Pt mesh as a counter electrode (CE), and an Ag/AgCl reference electrode (RE), was employed. 10 µl of C_3N_4 suspensions (1mg/ml) were drop-casted onto the WE (electrode area 0.07 cm^2). Measurements were performed in a

5 mM solution of potassium hexacyanoferrate (III) using as an electrolyte 100 mM PBS buffer (containing 100 mM KCl, Ph 7.4), A potential of 0.21 V (vs. reference) was applied with a perturbation of 10 mV, in the frequency range between 100 kHz and 10 mHz. The fitting of EIS data was performed using NOVA software v2.1.6 (Metrohm AutoLab B.V.). In the case of the time-resolved measurements, the same conditions were employed, but 10 µl of 0.1 mg/ml C_3N_4 suspensions were drop cast on the GCE.

Characterizations of CN_{Urea} and $oxCN_{Mel}$ materials

As shown in the TEM images in Figure S1), CN_{Urea} and $oxCN_{Mel}$ powder samples are characterized by small overlapped flakes.

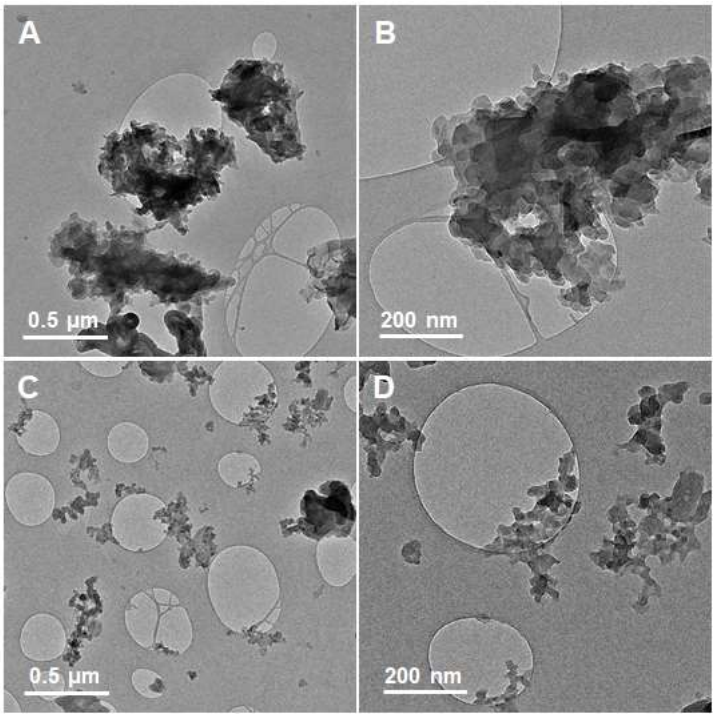

Figure S1. TEM images of powder samples: A), B) CN_{Urea} and C), D) $oxCN_{Mel}$.

The chemical structures of CN_{Urea} and $oxCN_{Mel}$ were futher investigated by X-ray diffraction (XRD), X-ray photoelectron spectroscopy (XPS), and Fourier transformed infrared (FT-IR) spectroscopy. The amount of elemental O in $oxCN_{Mel}$ powder, as measured by XPS, resulted much higher than that of CN_{Urea} (Table S1). This feature indicates the introduction of oxygen-containing functionalities during the oxidation process.

Table S1. Elemental composition of CN_{Urea} and $oxCN_{Mel}$, measured by XPS.

Sample	C (at%)	N (at%)	O (at%)
CN_{Urea}	46.6	52.2	1.2
$oxCN_{Mel}$	31.7	37.8	30.5

The XRD is a common fingerprint to determine the formation of C_3N_4 network containing tri-*s*-triazine units. The XRD patterns of both samples show two major peaks at ~13° and ~27°, corresponding to an intralayer distance between tri-*s*-triazine rings and an interlayer distance, respectively (Figure S2).[1]

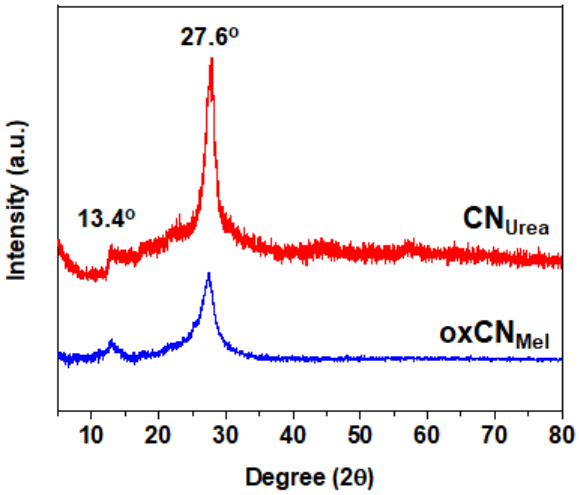

Figure S2. XRD patterns of CN_{Urea} and $oxCN_{Mel}$.

The suspensions of both samples in water showed fluorescence under irradiation using UV light and photoluminescence (PL) properties, obtained with an excitation of 300 nm (Figure S3). This PL feature is one of the common properties of C_3N_4 structures. However, the PL wavelength of $oxCN_{Mel}$ shifted to the lower wavelenght relative to that of CN_{Urea}. These PL data suggest that $oxCN_{Mel}$ possesses a different chemical structure from CN_{Urea}.

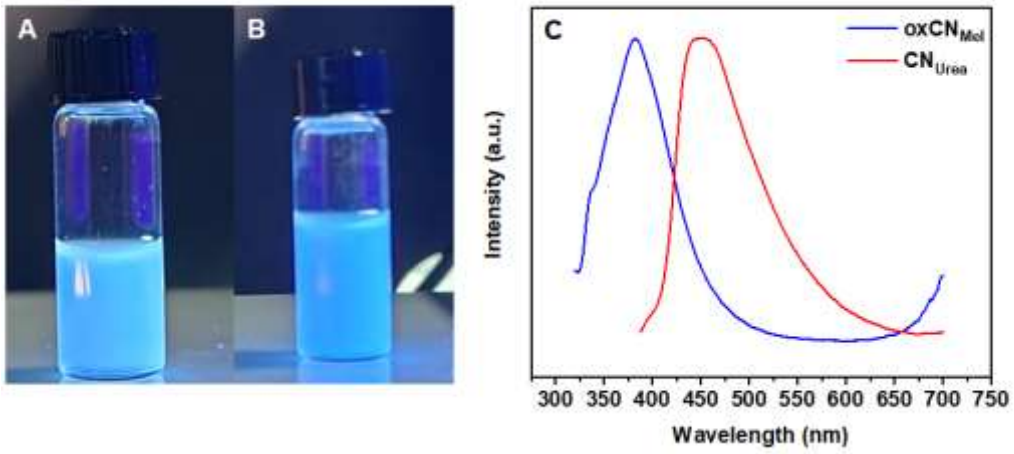

Figure S3. Fluorescent images of A) CN_{Urea} and B) $oxCN_{Mel}$. C) Photoluminescence spectra of CN_{Urea} and $oxCN_{Mel}$ excited at 300 nm.

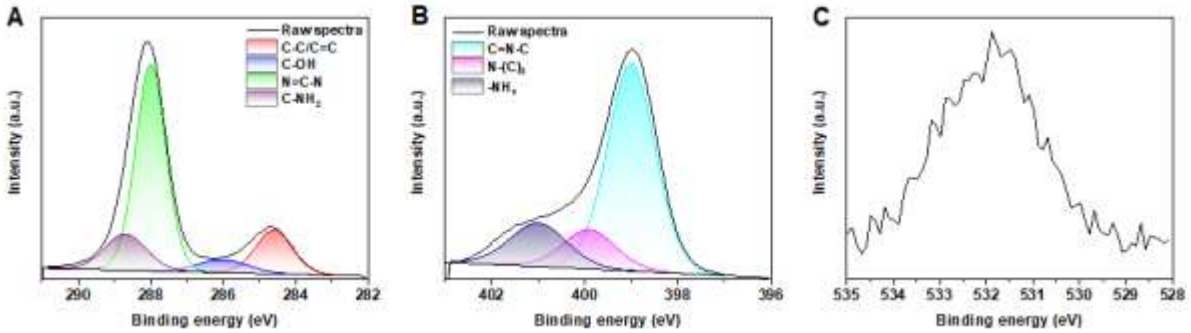

Figure S4. Deconvoluted high resolution XPS spectra of CN_{Urea}; A) C 1s, B) N 1s, and C) O 1s.

The XPS C and N 1*s* spectra of CN_{Urea} show a typical pattern for C_3N_4-based materials, revealing the formation of the C_3N_4 network (Figure 4A). The deconvoluted C 1s spectra have peaks at 284.6, 286.0, 287.0, 288.0, and 288.7 eV which correspond to C=C/C-C, C-O, N=C-N in tri-*s*-triazine rings, and C-NH_2 moieties, respectively (Figure S4). In the deconvoluted N 1s spectra, peaks at 399.0, 399.9, and 401.0 eV correspond to C-N=C, N-$(C)_3$, and NH_x groups, respectively (Figure S4B).[2] Trace of O atoms are also observed (Figure S4C). Although C_3N_4 materials that are completely condensed are not expected to exhibit an XPS peak at 284.6 eV for C=C/C-C, this peak has frequently been observed as a minor peak in previous studies, suggesting the presence of C impurities in the synthesized C_3N_4 materials.[3] This is a reason why larger amounts of C atoms were observed in the samples relative to that of theoretical C_3N_4 structures. XPS spectra of $oxCN_{Mel}$ are different from those of CN_{Urea}. The intensities of the peaks corresponding to the C(=O)O/C=O (XPS C 1s) and N–Hx groups (XPS N 1s) of $oxCN_{Mel}$ increased relative to that of CN_{Urea} (Figure S5). The N 1s peak for C=N-C group decreased after oxidation.

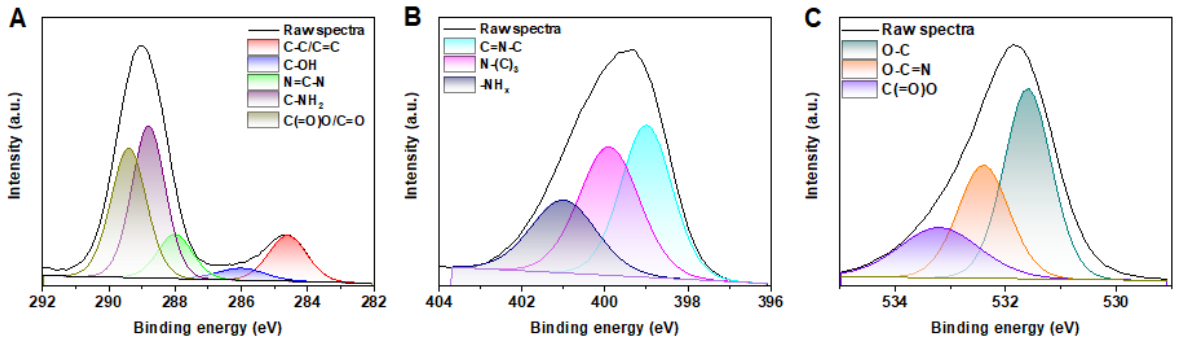

Figure S5. Deconvoluted high resolution XPS spectra of $oxCN_{Mel}$; A) C 1s, b) N 1s, and C) O 1s.

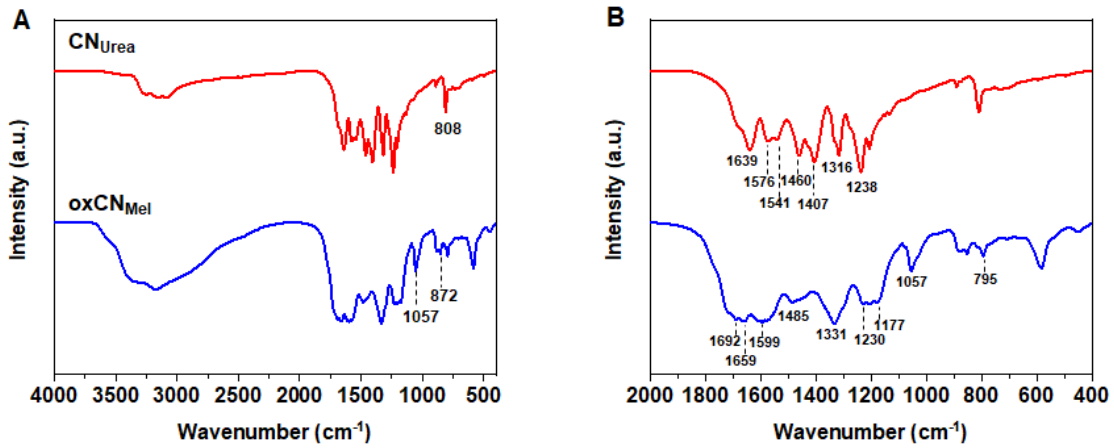

Figure S6. FT-IR spectra of CN_{Urea} and $oxCN_{Mel}$. A) Full range between 4000 and 400 cm^{-1} and B) selected range between 2000 and 400 cm^{-1}.

The FT-IR spectrum of CN_{Urea} shows typical features of C_3N_4 materials (Figure S6). Peaks at 1407, 1316, 1238 and 808 cm^{-1}, corresponding to a breathing mode of triazine rings, secondary bridging amines, and a C-N stretching of the tertiary nitrogen groups in tri-*s*-triazine rings, respectively (Figure S6). The peaks at 1639, 1576, 1541, 1460 and cm^{-1} correspond to the stretching modes of the tri-*s*-triazine ring. The broad bands between 3300 and 3000 cm^{-1} correspond to terminal/bridging amino groups (-NH_2 or -NH- groups). The spectrum of $oxCN_{Mel}$ shows stronger peaks around 3300 – 3000 and 1600 – 1700 cm^{-1}, corresponding to -NH_2/-NH- and C(=O)O/C=O groups, than that of CN_{Urea}. These spectra features indicate that the oxidatinn process forms -NH_2/-NH- and C(=O)O/C=O groups at the edge of $oxCN_{Mel}$ materials. The functional groups could be generated by decomposition of the N–C=N groups at the edges of the C_3N_4 networks during oxidation.[4]

Tyndall effect

To confirm the presence of fragments in the solutions both at the beginning and at the end of the degradation reaction, the Tyndall effect has been settled. This phenomenon is a light-scattering effect that appears when particles suspended in a medium are larger than the wavelength of light (650 nm) crossing the solution.[5] As descried by the red laser line, the presence of particles is constant for CN_{Urea} but, in comparison to the result obtained analyzing the first material, the Tyndall effect for $oxCN_{Mel}$ resulted less evident, suggesting the presence of fewer particles (**Erreur ! Source du renvoi introuvable.**).

Figure S7. Tyndall effect of CN_{Urea} and $oxCN_{Mel}$.

A

$$Fe^{3+} + H_2O_2 + h\nu \rightarrow Fe^{3+}OOH + H^+ \quad (1)$$

$$Fe^{3+}OOH \rightarrow Fe^{2+} + \cdot OOH \quad (2)$$

$$Fe^{2+} + H_2O_2 \rightarrow Fe^{3+} + \cdot OH + OH^- \quad (3)$$

$$Fe(OH)^{2+} + h\nu \rightarrow Fe^{2+} + \cdot OH \quad (4)$$

$$H_2O_2 + h\nu \rightarrow 2(\cdot OH) \quad (5)$$

B

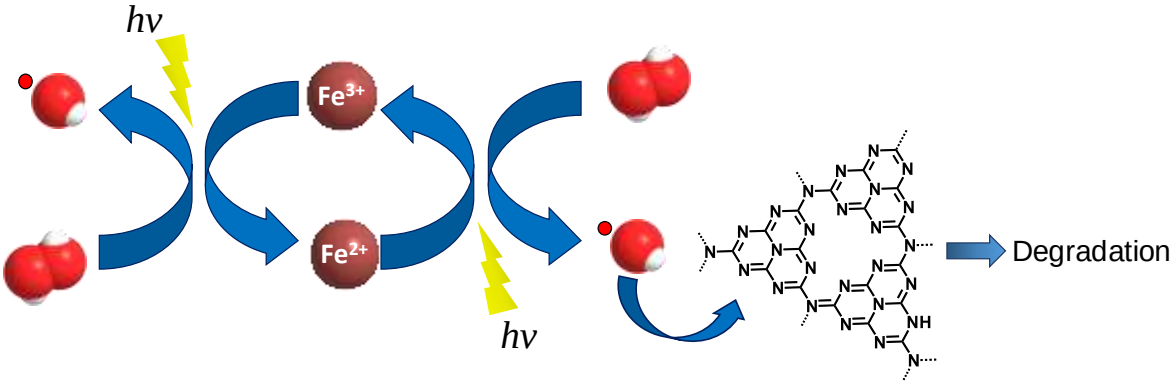

Figure S8. Equations involved in the generation of hydroxyl radicals during the photo-Fenton reaction (A), leading to the degradation of carbon nitrides (B).

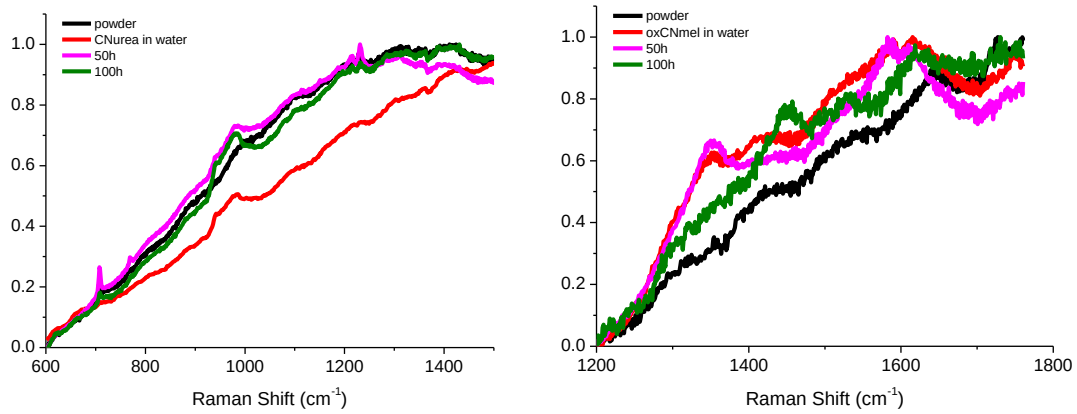

Figure S9. Raman spectra of CN_{Urea} (A) and $oxCN_{Mel}$ (B) at different time points during the photo-Fenton process.

Even if the materials were analyzed either depositing their powder or drying the dispersions at the different time points on the silica wafer, CN_{Urea} and $oxCN_{Mel}$ were highly autofluorescent masking their characteristic peaks. C_3N_4 are recognizable thanks to a peak at 707 cm^{-1}, attributed to the heptazine ring, and to a second peak at 1232 cm^{-1}, which represents the stretching vibration mode of C-N heterocycles.[6] In the spectra obtained from the analysis, these two characterizing peaks were very weak if not absent, thus hampering the observation of their evolution during the degradation process.

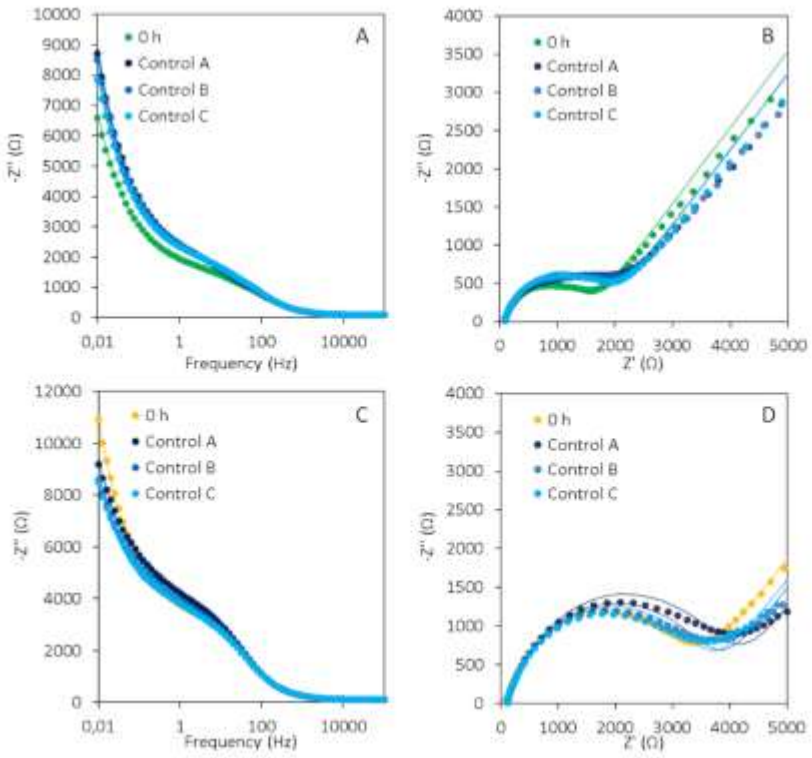

Figure S10. A) Bode plot of CN_{Urea} before the photo-Fenton reaction (0 h) and after the control reactions (Control A: with UV lamp, with Fe, without H_2O_2; Control B: with UV lamp, without Fe, without H_2O_2; Control C: with UV lamp, without Fe, with H_2O_2). The dots represent the experimental data, the line the fitting. B) Nyquist plot of CN_{Urea} before the photo-Fenton reaction (0 h) and after the control reactions. C) Bode plot of $oxCN_{Mel}$ before the photo-Fenton reaction (0 h) and after the control reactions. D) Nyquist plot of $oxCN_{Mel}$ before the photo-Fenton reaction (0 h) and after the control reactions.

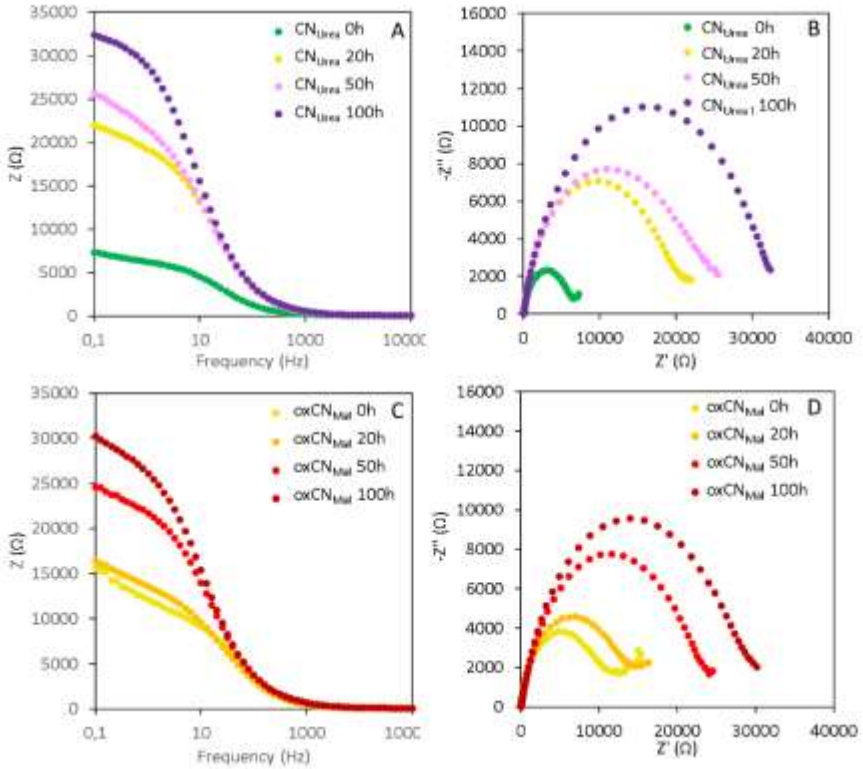

Figure S11. EIS measurements were obtained by drop casting 0.1 mg/ml of C_3N_4 on a GCE electrode, in a solution of 5 mM of $K_3[Fe(CN)_6]$. A potential of 0.21 V (vs. reference) was applied with a perturbation of 10 mV in a range of frequencies between 100 kHz and 10 mHz. A) Bode plot of CN_{Urea} at different time points (0, 20, 50, and 100 h) of the photo-Fenton reaction. B) Nyquist plot of CN_{Urea} at different time points (0, 20, 50, and 100 h) of the photo-Fenton reaction. C) Bode plot of $oxCN_{Mel}$ at different time points (0, 20, 50, and 100 h) of the photo-Fenton reaction. D) Nyquist plot of $oxCN_{Mel}$ at different time points (0, 20, 50, and 100 h) of the photo-Fenton reaction

References

1) J. Oh, Y. Shim, S. Lee, S. Park, D. Jang, Y. Shin, S. Ohn, J. Kim and S. Park, *J. Solid State Chem.*, 2018, **258**, 559–565.

2) J. Oh, J. M. Lee, Y. Yoo, J. Kim, S. J. Hwang and S. Park, *Appl. Catal. B*, 2017, **218**, 349–358.

3) D. Jang, S. Jeon, E. Y. Shin and S. Park, *Carbon Lett.*, 2023, **33**, 803–809.

4) J. Oh, R. J. Yoo, S. Y. Kim, Y. J. Lee, D. W. Kim and S. Park, *Chem. Eur. J.*, 2015, **21**, 6241–6246.

5) J. Stetefeld, S. A. McKenna and T. R. Patel, *Biophys Rev.*, 2016, **8**, 409–427.

6) M. Wang, F. Ma, Z. Wang, D. Hu, X. Xu and X. Hao, *Photonics Res,* 2018, **6**, 307.